The Meteoritical Society

Meteoritics & Planetary Science 1–12 (2017)
doi: 10.1111/maps.12880

A new high-precision $^{40}Ar/^{39}Ar$ age for the Rochechouart impact structure: At least 5 Ma older than the Triassic–Jurassic boundary

Benjamin E. COHEN[1,2,*], Darren F. MARK[1,3], Martin R. LEE[2], and Sarah L. SIMPSON[2]

[1]NERC Argon Isotope Facility, Scottish Universities Environmental Research Centre, Rankine Avenue, East Kilbride G75 0QF, UK
[2]School of Geographical and Earth Sciences, University of Glasgow, Glasgow G12 8QQ, UK
[3]Department of Earth and Environmental Sciences, University of St Andrews, St Andrews KY16 9AL, UK
[*]Corresponding author. E-mail address: ben.cohen@glasgow.ac.uk

(Received 19 August 2016; revision accepted 19 March 2017)

Abstract–The Rochechourt impact structure in south-central France, with maximum diameter of 40–50 km, has previously been dated to within 1% uncertainty of the Triassic–Jurassic boundary, at which time ~30% of global genera became extinct. To evaluate the temporal relationship between the impact and the Triassic–Jurassic boundary at high precision, we have re-examined the structure's age using multicollector ARGUS-V $^{40}Ar/^{39}Ar$ mass spectrometry. Results from four aliquots of impact melt are highly reproducible, and yield an age of 206.92 ± 0.20/0.32 Ma (2σ, full analytical/external uncertainties). Thus, the Rochechouart impact structure predates the Triassic–Jurassic boundary by 5.6 ± 0.4 Ma and so is not temporally linked to the mass extinction. Rochechouart has formerly been proposed to be part of a multiple impact event, but when compared with new ages from the other purported "paired" structures, the results provide no evidence for synchronous impacts in the Late Triassic. The widespread Central Atlantic Magmatic Province flood basalts remain the most likely cause of the Triassic–Jurassic mass extinction.

INTRODUCTION

Accurate and precise ages for impact structures are crucial to evaluate the geological effects of these sudden cataclysmic events (Jourdan et al. 2009a, 2012). At the Rochechouart impact structure, France, the timing of impact has been progressively refined over the past 45 yr, with steadily improving precision and accuracy reflecting the refinement and advances in mass spectrometry and equivalent technology, sample selection, and preparation techniques (Table 1). The existing most precise age for the Rochechouart impact event is 203 ± 2 Ma (2σ; Schmieder et al. 2010), recalculated using the decay constants and Fish Canyon sanidine standard age from Renne et al. (2011) (Table 1). This age of 203 ± 2 Ma overlaps with the Triassic–Jurassic boundary age of 201.33 ± 0.27 Ma (2σ full external uncertainties; Schoene et al. 2010; Gradstein et al. 2012). The mass extinction that occurred at this time was responsible for the loss of ~30% of global genera (Rohde and Muller 2005), and therefore it is crucial to determine the trigger(s) for the extinction, such as volcanism versus impact. However, the Schmieder et al. (2010) Rochechouart age of 203 ± 2 Ma, with a 2σ uncertainty of ±1% (Table 1), lacks the precision necessary to evaluate if the impact event predates, postdates, or is synchronous with the Triassic–Jurassic boundary (Lambert 2010; Jourdan et al. 2012).

Schmieder et al. (2010) recognized that their age is insufficiently precise to fully assess a temporal link between the impact and extinction event. They also pointed out that the relatively small size of Rochechouart (<50 km diameter) may suggest that this event was too small to have caused an extinction. Nevertheless, some studies have used the apparent temporal synchronicity between impact and extinction to investigate a potential causal link between the two events (e.g., Smith 2011), and therefore the age of Rochechouart requires reassessment. Furthermore, the Rochechouart structure has been proposed as a member of a multiple impact event, comprising either the

Table 1. Ages for the Rochechouart impact structure.

References	Reported age ± 2σ (Ma)	Recalculated age ± 2σ (Ma)	Method	Rock type and locality analyzed
This study	206.92 ± 0.32	206.92 ± 0.32	$^{40}Ar/^{39}Ar$ step heat	Impact melt, Babaudus
Eitel et al. (2014)	Reversed polarity	Reversed polarity	Paleomagnetism	Impact melt-bearing breccia, several localities
Schmieder et al. (2010)	201 ± 2	203 ± 2	$^{40}Ar/^{39}Ar$ step heat	Impact-shocked gneiss, near Videix
Carporzen and Gilder (2006)	210–220	210–220	Paleomagnetism	Impact melt-bearing breccia, four sites
Kelley and Spray (1997)	214 ± 8	217 ± 8	$^{40}Ar/^{39}Ar$ spot fusion	Pseudotachylyte, Champagnac quarry
Reimold and Oskierski (1987)	186 ± 9	190 ± 50	Rb-Sr	Impact melt
Wagner and Storzer (1975)	198 ± 25	198 ± 25	Apatite fission track	Green impact melt-bearing breccia, Chassenon
Wagner and Storzer (1975)	206 ± 39	206 ± 39	Glass fission track	Green impact melt-bearing breccia, Chassenon
Lambert (1974)	165 ± 5	170 ± 5	K-Ar (minimum age)	Impact melt glass
Kraut and French (1971)	154 ± 8	159 ± 8	K-Ar (minimum age)	Impact melt, Babaudus
Kraut and French (1971)	173 ± 8	178 ± 8	K-Ar (minimum age)	Impact melt, Babaudus
Pohl and Soffel (1971)	Late Triassic	Late Triassic	Paleomagnetism	Red and green impact melt-bearing breccia, impact melt

All K-Ar and $^{40}Ar/^{39}Ar$ ages have been recalculated to the decay constants of Renne et al. (2011). The Rb-Sr age has been recalculated to the decay constants of Rotenberg et al. (2012). Uncertainties incorporate full external uncertainties, including uncertainties in the decay constants. This is to enable comparisons between isotopic decay systems, in particular U-Pb, as the age of the Triassic–Jurassic boundary is determined via this isotopic system (Schoene et al. 2010).

Rochechouart, Manicouagan, Lake Saint Martin, Obolon, and Red Wing structures (Spray et al. 1998), or the Rochechouart and Puchezh-Katunki structures (Schmieder et al. 2010). Testing these multiple impact hypotheses requires re-examination in light of new high-precision age results from Rochechouart and the other purportedly contemporaneous structures.

On a more regional scale, the Rochechouart impact event has also been potentially linked to Late Triassic seismite and tsunamite deposits in the United Kingdom, which are separated from the impact site by a distance of >600 km (Schmieder et al. 2010; Smith 2011). These deposits cover an area of >250,000 km^2, and are found in the Cotham Member, part of the Lilstock Formation, within the Rhaetian (209.5–201.3 Ma) Penarth Group (Simms 2002, 2007).

In this study, we have used multicollector noble gas mass spectrometry (e.g., Mark et al. 2009) to generate a high-precision $^{40}Ar/^{39}Ar$ age for Rochechouart and re-examine the temporal relationship between this impact and the Triassic–Jurassic boundary. This new age can also be used to explore any relationship between the Rochechouart impact event and craters and impactitie deposits elsewhere. Precise dating of crater formation via the targeting of high-temperature rocks rather than hydrothermal minerals (i.e., Schmieder et al. 2010) may also help to constrain the duration of the postimpact hydrothermal system (i.e., Δt between these two ages), which has recently been shown to have supported a microbial biosphere (Simpson et al. 2017).

Rochechouart Structure and Sample Selection

Rochechouart is a moderate-sized impact structure, with a maximum original diameter of 40–50 km (Lambert 2010; Sapers et al. 2014), although postimpact erosion has reduced the exposure to approximately 24 km (Lambert 2010). The structure contains a variety of impactites, ranging from melt-rich to melt-poor material, including impact melt, impact melt-bearing breccia, lithic impact breccia, and ash-sized fallout debris (Lambert 2010; Sapers et al. 2014) (Fig. 1). The target rocks were largely igneous and metamorphic lithologies of the Massif Central, including felsic gneiss, metabasic gneiss, amphibolite, and intrusions of diorite and granitoid magmas (Lambert 2010) (Fig. 1). These metamorphic and igneous basement rocks have cooling ages that range from 400 to 300 Ma (Reimold and Oskierski 1987; Lambert 2010; and references therein). The impact occurred close to the Mesozoic shoreline, as marine deposits of the Late Triassic Aquitaine Basin are preserved 15–20 km west of the center of the impact structure—well within the 40–50 km full crater diameter (Lambert 2010) (Fig. 1). However, due to erosion of the

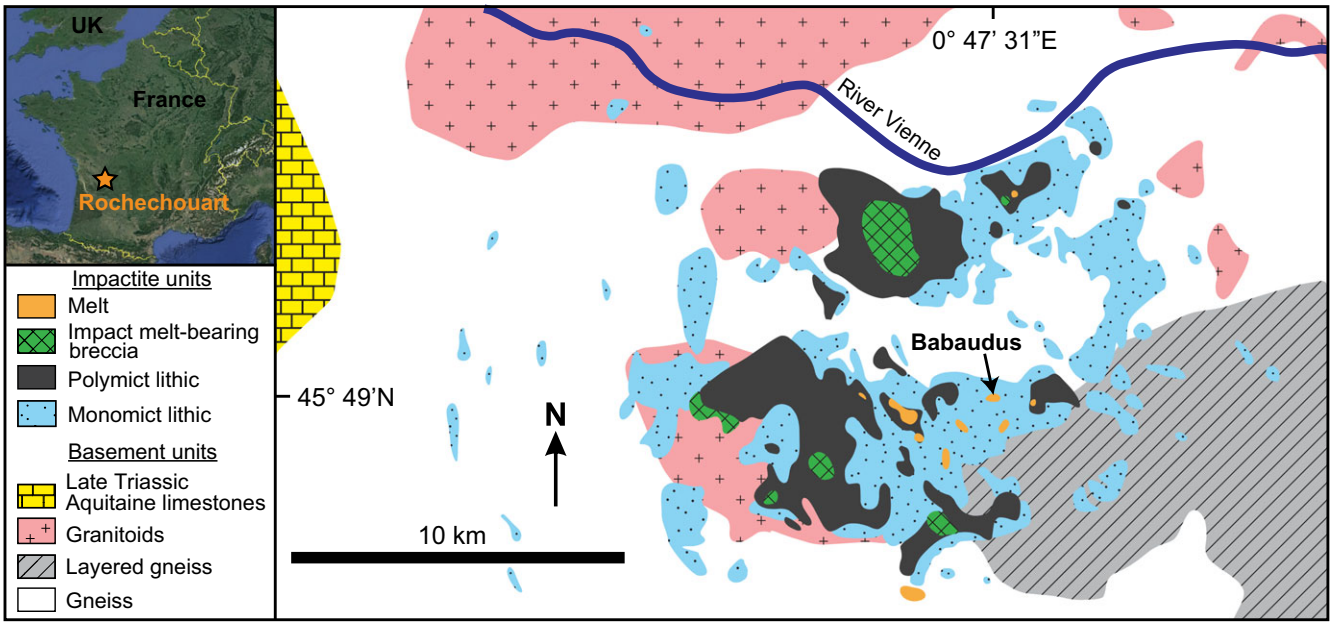

Fig. 1. Map of Rochechouart impact structure, modified from Lambert (2010). Basement gneiss and granitoid intrusions have metamorphic and igneous ages ranging from 400 to 300 Ma. The preserved edge of the Late Triassic Aquitaine Basin lies 15–20 km west of the structure's center. Impactite deposits are preserved in the center of the structure, and comprise monomict and polymict breccia, impact melt-bearing breccia, and impact melt. The regional map is from Google Earth.

edge of this basin and the removal of crucial parts of the sedimentary record, it is unknown whether the impact occurred in a terrestrial or shallow marine setting (Lambert 2010).

As regards to sample selection, $^{40}Ar/^{39}Ar$ dating of impact structures can be compromised if the rocks analyzed contain clasts of the target lithologies, which if not fully degassed during crater formation will retain older (i.e., inherited) ^{40}Ar (e.g., as discussed by Jourdan et al. 2007a; Mark et al. 2014). To avoid potential complications from target rock clasts, we therefore focused our study on the K-feldspar bearing impact melt at Babaudus, which contains the highest percentage of melt and smallest percentage of preimpact clasts of all of the Rochechouart impactite products (Sapers et al. 2014). A sample of fresh Babaudus melt was obtained from the Réserve Naturelle de l'Astroblème de Rochechouart–Chassenon. The Babaudus outcrop is only 1–2 m thick and a few hundred meters wide (Lambert 2010), and is located at 45°49′00.63″N, 0°47′31.04″E. Our sample (Fig. 2a) comprised a block ~8 cm long by ~1 cm thick, sawn from a > 20 cm fragment.

METHODS

In order to characterize the mineralogy and grain size of the melt rock, and assess the suitability for $^{40}Ar/^{39}Ar$ analysis, the Babaudus sample was studied by conventional petrographic microscopy and by scanning electron microscopy (SEM) at the University of Glasgow. Prior to the SEM work, the sample was carbon coated, then backscattered electron images and electron dispersive X-ray analyses were obtained using a Carl Zeiss Sigma SEM operated in high-vacuum mode and at 20 kV/~2 nA.

For $^{40}Ar/^{39}Ar$ analysis, the impact material was crushed and sieved to <750 μm using an agate mortar and pestle, then cleaned for ~60 min in deionized water plus ethanol in an ultrasonic bath at <50°C. After washing, the material was oven-dried (<50°C), and resieved to remove material that was <250 μm in size. The impact melt separate (250–750 μm) was hand-picked under a binocular microscope.

The impact melt material was loaded into an 11-well aluminum disk, along with the following age standards: Fish Canyon sanidine (~500 μm crystals; Morgan et al. 2014) and GA1550 biotite (250–500 μm crystals; McDougall and Wellman 2011). The canister was irradiated for 20 h at the 1 MW Cd-lined In-Core Irradiation Tube TRIGA research reactor at the Oregon State University, USA. Multiple aliquots of the impact melt sample and age standards were placed in 2 mm diameter and 2 mm deep circular holes in a steel palette, which was loaded into a laser chamber of a noble gas ultrahigh vacuum extraction line and baked at

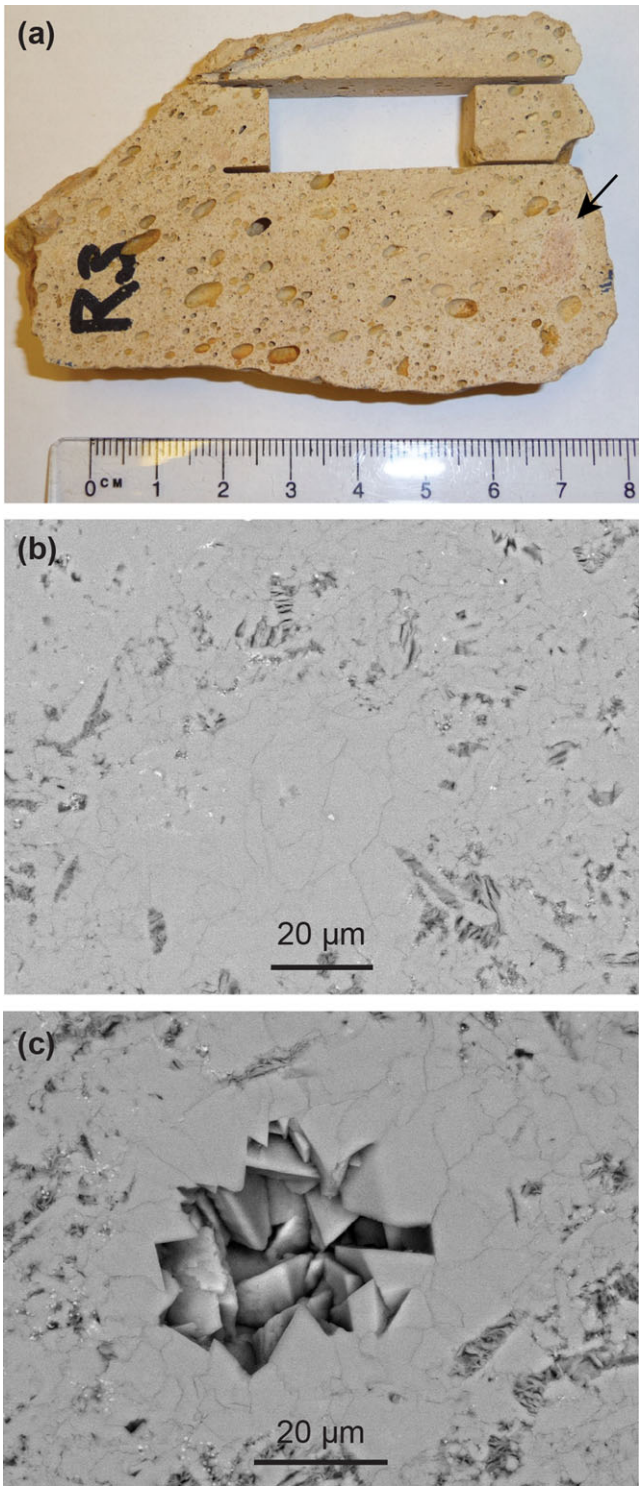

Fig. 2. Petrography of the Babaudus impact melt. a) Hand sample showing the highly vesicular character of the rock. The bulk of the sample is comprised of buff to pale yellow material, predominantly K-feldspar, whereas some of the vesicles are lined with a very thin layer of clay and goethite. A single clast is present in this slab (a < 1 cm wide sphere of pale-pink material, arrowed, and avoided when sampling for $^{40}Ar/^{39}Ar$), demonstrating the rarity of basement clasts in the Babaudus melt. b, c) Backscattered electron images showing that the Babaudus impact melt is dominantly (90%) composed of K-feldspar. Individual feldspar crystals are on average 25 µm in size, but form a closely packed interlocking network suitable for $^{40}Ar/^{39}Ar$ analysis. Euhedral K-feldspar crystals line a small vesicle in (c). In both SEM images, the darker gray and platy material is smectite clay, whereas the brightest gray phase represents submicrometer-sized crystals of titanomagnetite.

<150°C for ~2 days. To ensure sufficient gas was released for precise analysis, each of the Rochechouart aliquots contained 4–6 fragments, while the Fish Canyon and GA1550 aliquots contained two crystals per well. Care was taken to ensure the samples were presented as a monolayer (Barfod et al. 2014).

The samples and age standards were analyzed at the Scottish Universities Environmental Research Centre (SUERC), United Kingdom, on a GVI ARGUS-V multicollector mass spectrometer (Mark et al. 2009) with a measured sensitivity of 7×10^{-14} mol V^{-1}. A Photon Machines 10.4–10.8 µm CO_2 laser was used to heat the age standards and samples for 60 s per step, using a 2 mm diameter circular flat beam. Fish Canyon sanidine age standards were fused in a single step at 11.25 Watts, while the Rochechouart samples and GA1550 were incrementally heated. The released gases were cleaned for 5 min by exposure to three SAES GP50 getters, two operated at ~450°C and one at room temperature. After cleaning, the gas was inlet to the mass spectrometer, where a fourth getter (NP10) operated at room temperature was located near the ionizing source. Additional details of mass spectrometer specifications and operations are found in Mark et al. (2009).

Full-system background measurements were run before every analysis. ^{40}Ar signal sizes for Rochechouart samples and Fish Canyon sanidine were typically a factor of 100–1000 above blank levels (Table S1 in supporting information). Air shots were run frequently to monitor mass discrimination (Table S1). All data regression was undertaken in MassSpec software, version 8.131. Mass spectrometer discrimination was calculated per AMU using the power law, and an atmospheric $^{40}Ar/^{36}Ar$ value of 298.56 ± 0.31 (Lee et al. 2006), which has been independently confirmed by Mark et al. (2011). We used the age for Fish Canyon sanidine of (28.294 ± 0.036 Ma [1σ]) and ^{40}K decay constants from Renne et al. (2011); details of other decay constants and irradiation parameters are in Table S1. All uncertainties in Table S1 are reported at the one-sigma level, while all uncertainties in the text and figures are reported at the two-sigma level. Age uncertainties in the paper are reported as the age ± *Y*/

Z, where Y is the analytical precision and Z is the full external precision, including the uncertainties from both the Fish Canyon sanidine age standard and decay constants.

As a further test of the reliability of our J values determined from the analyses of the Fish Canyon sanidine age standard, we analyzed four aliquots of the international standard GA1550 biotite (McDougall and Wellman 2011) as an unknown sample. These GA1550 analyses yielded a weighted mean age of 99.99 ± 0.21/0.25 Ma (2σ; n = 20), which is within uncertainty of the accepted age for this sample, of 99.738 ± 0.208 Ma (2σ; Renne et al. 2011). This GA1550 biotite data therefore demonstrate the accuracy of our determination of the irradiation J value.

RESULTS

Petrographic Results

Our selected Babaudus impact melt sample (Unit 5 of Sapers et al. 2014) is classified as a clast-poor to clast-free impact melt rock, with a shock level of IV (rock glasses and/or crystallized melt rock) in the International Union of Geological Sciences impactite classification scheme (Stöffler and Grieve 2011). The sample is a buff to pale yellow colored fine-grained crystalline rock with abundant vesicles (Fig. 2a). Vesicles are often elongated, which suggests that the impact melt flowed during cooling (Lambert 2010). The vesicles can be up to >10 mm long, but in the fragment analyzed they are <4 mm long (Fig. 2a). Lithic clasts are rare (Fig. 2a); they are quartzofeldspathic, comprise <10 volume % of the rock, and tend to be rounded, with evidence for partial melting and assimilation.

The crystalline groundmass has a mean grain size of 25 μm, and consists almost entirely of an interlocking network of K-feldspar crystals (Fig. 2). This close crystal packing minimizes Ar loss via weathering, and also limits the effects of recoil during neutron irradiation (see further information in the Discussion section). The euhedral shape of the K-feldspar crystals is best observed on vesicle margins (Fig. 2). The fine grain size of K-feldspar in our Babaudus impact melt sample indicates that this material cooled and crystallized rapidly after the impact event.

The Babaudus impact melt sample contains minor amounts (<10 volume %) of smectite and goethite (Fig. 2). These phases form as a result of interaction with low-temperature fluids, either during postimpact hydrothermal cooling, or alternatively during more recent subaerial weathering. The Babaudus material also contains minor amounts of submicron-sized Fe-Ti oxides (Sapers et al. 2014) (Fig. 2).

$^{40}Ar/^{39}Ar$ Results

The Babaudus impact melt sample was analyzed in four aliquots, and the results are highly reproducible (Fig. 3). Except for the lowest temperature steps, the % radiogenic ^{40}Ar ($^{40}Ar^*$) yields are high (>99%), indicating little contribution from atmospheric ^{40}Ar (Fig. 3). The material analyzed lacks calcium, as shown by the $^{37}Ar_{Ca}$ analyses that are within uncertainty or only marginally higher than zero (Table S1). This observation is important because the granitoid and gneiss basement rocks at Rochechouart (Fig. 1) typically contain >1 wt% of CaO, which is contained in plagioclase and pyroxene, and 3–6 wt% K_2O (Lambert 2010). The absence of ^{37}Ar (and therefore Ca) in the Babaudus results is therefore excellent evidence that the aliquots analyzed are free of Ca-bearing basement clasts. $^{38}Ar_{Cl}$ contents are also within uncertainty of zero, indicating that the material analyzed does not contain measurable chlorine.

The low-temperature steps yield ages of <190 Ma (Fig. 3; Table S1 in supporting information). This finding is consistent with the presence of <10% smectite clays within the Babaudus impact rocks (Fig. 2), as $^{40}Ar^*$ in smectite can be partially degassed at low (ambient) temperatures (McDougall and Harrison 1999), which would produce younger apparent ages. Fortunately the bulk of these clays were removed by ultrasonic cleaning prior to analysis. Fragments containing clay were also avoided during hand picking.

The ages obtained for the middle- and high-temperature steps rapidly stabilize to form plateaus containing 5–11 heating steps that overlap at the 2σ confidence level. The plateaus have MSWD less than two, probability values of >0.09, and comprise >60% of the ^{39}Ar released (Fig. 3). The plateaus therefore fulfill the standard criteria developed for igneous rocks retaining their primary crystallization age (McDougall and Harrison 1999). We have therefore combined the analyses from all plateau steps, to obtain a combined weighted mean age of 206.92 ± 0.20/0.32 Ma, with MSWD of 1.65 (n = 32; 2σ full analytical/external uncertainties). Isochron analysis of the results combined from all four aliquots also yields a concordant age of 206.96 ± 0.21/0.33 Ma, with MSWD of 0.63 (Fig. 3). As the isochron is based on the plateau steps only, which all have ≫99% $^{40}Ar^*$, there is little spread on the isochron, resulting in an imprecise determination of initial $^{40}Ar/^{36}Ar$ of 480 ± 260 (Fig. 4). The highest temperature steps from Babaudus yielded ages just beyond 2σ uncertainty from the plateaus (206–202 Ma; Fig. 3) and, as discussed below, most likely reflect minor amounts of ^{39}Ar recoil redistribution within this sample.

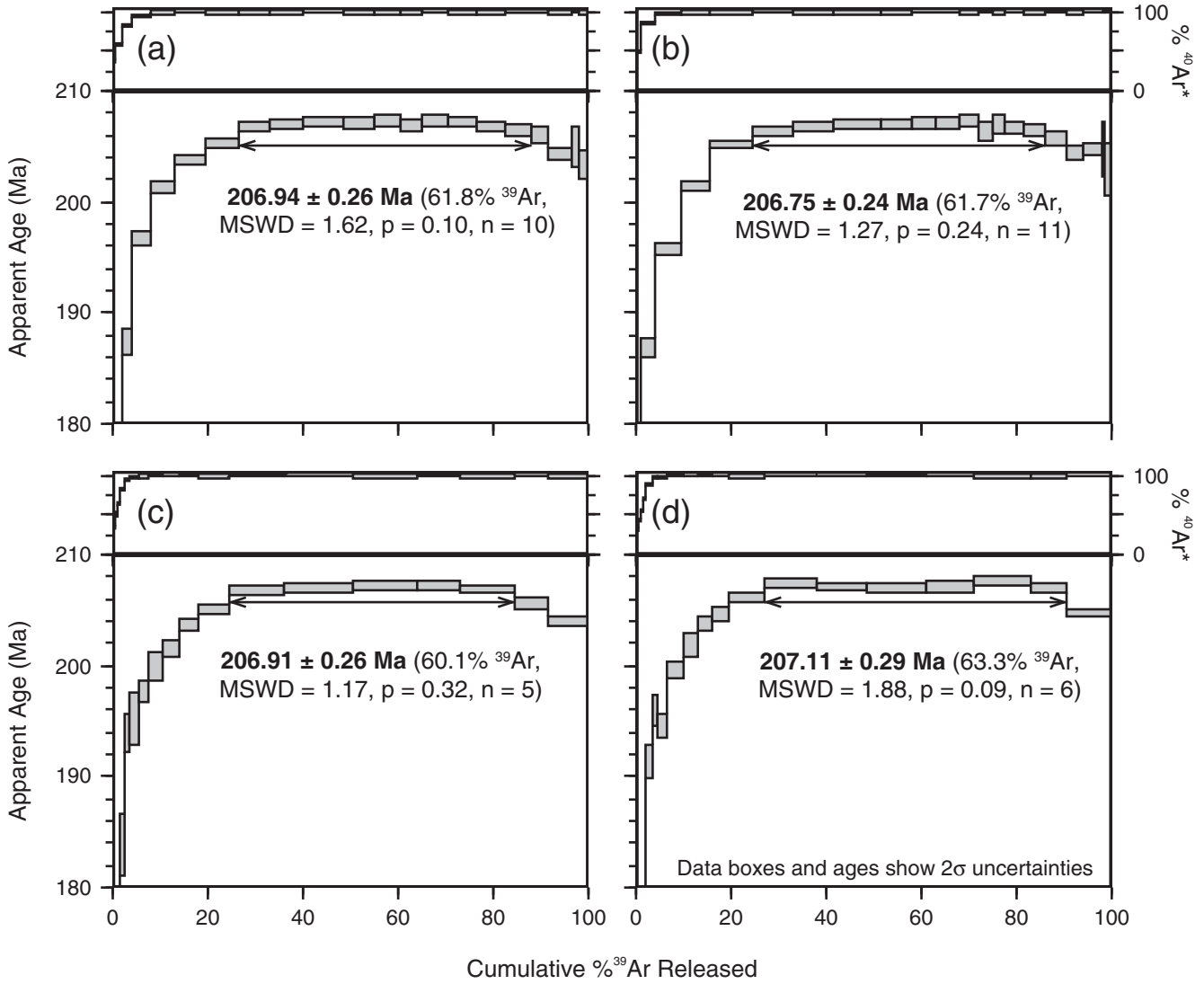

Fig. 3. a–d) $^{40}Ar/^{39}Ar$ incremental-heating analyses of the Babaudus impact melt. The results are highly reproducible between the four aliquots, giving high $\%^{40}Ar^*$ yields and plateau ages representing >60% of the ^{39}Ar released. Low-temperature steps yielded younger ages, consistent with the <10% smectite clay found in this impact melt sample.

DISCUSSION

Challenges in Dating Impactites

Dating of impact rocks can potentially be problematic owing to the presence of excess ^{40}Ar, and recoil of ^{39}Ar and/or ^{37}Ar (Jourdan et al. 2009a). Potassium and/or Ar may also be lost by postimpact hydrothermal alteration or weathering (Jourdan et al. 2009a). The issue of excess Ar can be particularly troublesome for impacts with target rocks comprised of old granitic material, as it is more difficult for high-viscosity melts (e.g., of a granitic composition) to be fully degassed of Ar compared to low-viscosity melts (e.g., mafic compositions) (Webb and McDougall 1967; Jourdan et al. 2007a, 2011). This difference arises because the viscosity of a melt significantly affects Ar diffusion, and thus, resetting the Ar geochronologic "clock" at the time of impact. Thus, a primary challenge to $^{40}Ar/^{39}Ar$ dating of impact structures is incomplete degassing of $^{40}Ar^*$ accumulated in K-bearing target rocks (inherited ^{40}Ar), for example, at the Tswaing crater in Africa (Jourdan et al. 2007a). Nondegassed or incompletely $^{40}Ar^*$-degassed target rock can become incorporated in an impact melt, and the degree of $^{40}Ar^*$-degassing of the K-bearing minerals is dependent upon (1) the size and thermal conductance of the rock; (2) the Ar diffusion properties of the K-bearing minerals; (3) the size of the K-bearing minerals; and (4) the temperature and duration of shock

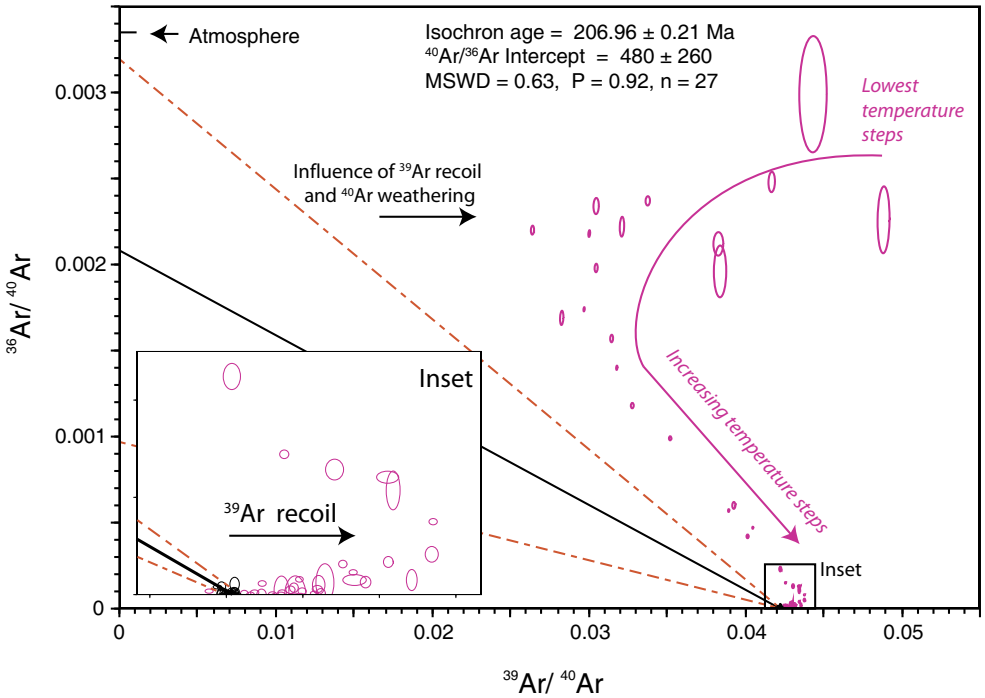

Fig. 4. Inverse isochron, combining data from all four aliquots. The 27 plateau steps (black) form a tight cluster near the *x*-axis (best viewed on the inset), reflecting their very high $^{40}Ar^*$ content. As a result, the isochron has a precise age, but imprecise initial $^{40}Ar/^{36}Ar$ intercept. Nonplateau steps (magenta) lie to the right of the isochron, mostly as a result of ^{39}Ar recoil. The lowest temperature steps, reflecting degassing of smectite clay (Figs. 2 and 3), also lie to the right of the isochron, and probably reflect a combination of ^{39}Ar loss due to recoil and ^{40}Ar loss due to weathering.

metamorphism, latent heat effects in a melt, or subsequent hydrothermal heating (Jourdan et al. 2007a). In addition, the effects of shock metamorphism in target rocks are notoriously heterogeneous on micrometer to multimeter scales (Collins et al. 2008; Osinski and Pierazzo 2012).

In the case of Rochechouart, the target rocks were a mixture of felsic and more mafic lithologies (Fig. 1) (Lambert 2010). Chemical analyses (n = 45) of Rochechouart impact melts show an average of 66.0 wt% SiO_2, 0.34 wt% Na_2O, and 10.19 wt% K_2O (Lambert 2010). This composition is equivalent to a trachytic melt, which is important as trachytes have a lower viscosity than granitic/rhyolitic melts (at the same temperature), due to the lower SiO_2 and greater alkali contents in trachytic magmas (Giordano et al. 2004), and thus allowing for efficient degassing of the Rochechouart impact melts. Rochechouart also has an advantage for $^{40}Ar/^{39}Ar$ dating that, at the time of impact, the basement rocks were relatively young, with only 100–200 Ma separating the metamorphism/intrusion ages of the target rocks and the subsequent impact event. The Rochechouart basement rocks would therefore have contained less original $^{40}Ar^*$ than the target rocks of the Tswaing crater, which were 2050 Ma granites (Jourdan et al. 2007a). Size differences between the Rochechouart and Tswaing craters (maximum diameters of 50 km and 1.13 km, respectively) mean that the far more energetic Rochechouart event would have been associated with greater intensities of shock and heating compared to Tswaing. Furthermore, grain boundaries between crystals in the Babaudus material (Figs. 2b and 2c) would have enhanced volatile migration as the impact melt was cooling, and the presence of abundant vesicles in the Babaudus sample (Fig. 2a) indicates that trapped gases had time to escape from the melt, thus minimizing problems due to inherited Ar.

Regarding recoil, the dense interlocking and close packing of K-feldspar crystals in the Babaudus melt rock would have limited the effects of ^{39}Ar ejection during neutron irradiation (e.g., Jourdan et al. 2007b). This is because atoms recoiling from one crystal would have been implanted into an adjacent K-feldspar crystal (i.e., recoil redistribution rather than loss; Fig. 5). In this regard, analysis of the Babaudus impact melt rock is similar to dating fine-grained volcanic rocks, which frequently have groundmass crystals <25 μm in size, and are routinely analyzed by $^{40}Ar/^{39}Ar$ (e.g., Koppers et al. 2000, 2012). Nevertheless, due to the mineralogy

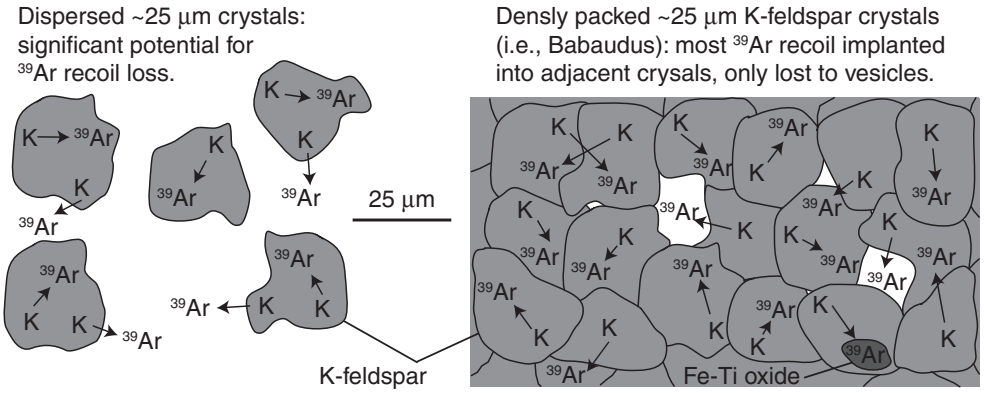

Fig. 5. Schematic diagram demonstrating why, despite the 25 μm mean crystal size, ^{39}Ar recoil is largely mitigated in the Babaudus sample (right image), due to the closely packed interlocking network of crystals. Voids are white, K-feldspar crystals are mid-gray, and Fe-Ti oxides are dark gray.

and grain size of the Babaudus sample (Fig. 2), some recoil redistribution and loss is unavoidable, and is indeed observed in the ^{40}Ar/^{39}Ar results (Figs. 3 and 4). ^{39}Ar recoiled into the vesicles can be lost (if the vesicle is connected to the outside of the rock) or trapped in the vesicles (if the vesicle is airtight) (i.e., micropermeability versus microporosity), and has likely influenced the low-temperature steps. Meanwhile, the highest temperature steps also show a slight disturbance, with ages younger than the plateau (Fig. 3). This behavior is observed in many rocks (e.g., Jourdan et al. 2009b; Koppers et al. 2012), and may also be due to recoil redistribution, e.g., ^{39}Ar implanted into Fe-Ti oxides (Figs. 2 and 5).

The influence of ^{39}Ar recoil loss is most evident in the isochron analysis, as this phenomenon shifts analyses to the right of an inverse isochron (Koppers et al. 2000) (Fig. 4). Despite the effects of recoil on some steps, 27 analyses (i.e., the plateau-forming steps) form a tight cluster on the isochron diagram, demonstrating that these steps were unaffected by recoil, and are thus suitable to calculate an ^{40}Ar/^{39}Ar cooling age for the Babaudus impact melt.

Age of the Rochechouart Structure and Its Implications

Given the reproducibility of our ^{40}Ar/^{39}Ar results in four aliquots, the absence of preimpact clasts in the analyzed Babaudus aliquots, and the presence of four concordant ^{40}Ar/^{39}Ar plateau ages containing >60% of the ^{39}Ar released, we consider the age of 206.92 ± 0.20/0.32 Ma (2σ full analytical/external uncertainties) as a reliable crater formation age for the Rochechouart impact.

An additional constraint on the impact age is provided by paleomagnetic analyses of impact melt-bearing breccias from the Rochechouart structure (Eitel et al. 2014). Thirty samples possessing mostly titanium-free hematite as the magnetic remanence carrier have solely reverse-polarity directions, and also pass data selection criteria from Thellier–Thellier experiments (Eitel et al. 2014). These results demonstrate that the impact occurred during a period of reversed magnetic polarity (Eitel et al. 2014). According to the Geologic Time Scale 2012 (Gradstein et al. 2012), there were relatively few periods of reverse-polarity in the Rhaetian, which considerably narrows the range of options for the paleomagnetic age of Rochechouart (Fig. 6). Using the most recently published Geologic Time Scale (Gradstein et al. 2012), our Rochechouart age overlaps a period of reversed polarity, thus supporting the conclusion that our ^{40}Ar/^{39}Ar result accurately records the impact age (Fig. 6). We note, however, that the exact timing of paleomagnetic reversals in the Late Triassic are still being refined (Gradstein et al. 2012).

We can now use this increased temporal precision for the age of impact to examine several aspects of the geology of Rochechouart: its relationship with the Triassic–Jurassic boundary, any temporal links with other impact structures and regional geological events, and the longevity of postimpact hydrothermal activity within the impact structure.

The Triassic–Jurassic boundary has been dated by single-crystal zircon U-Pb chemical abrasion isotope dilution thermal ionization mass spectrometry (CA-ID-TIMS) at 201.33 ± 0.27 Ma (2σ, full external uncertainties; Schoene et al. 2010; Gradstein et al. 2012). The ^{40}Ar/^{39}Ar results from our study therefore demonstrate that the Rochechouart impact predates the Triassic–Jurassic boundary by 5.6 ± 0.4 Ma. As a consequence of this newly obtained Rochechouart impact age and recent chronology of other impact structures (Jourdan et al. 2009a, 2012), there is now no

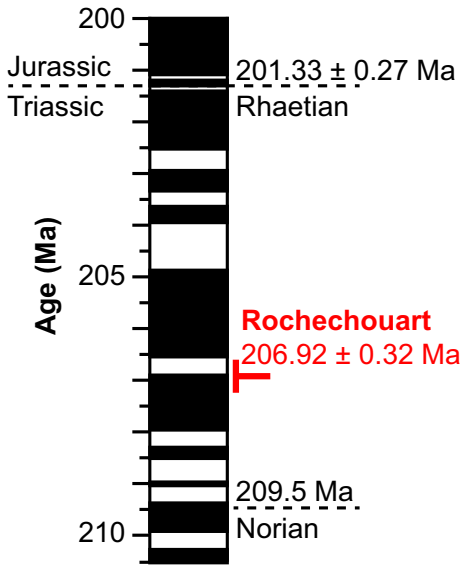

Fig. 6. Our Rochechouart $^{40}Ar/^{39}Ar$ age in comparison to the Late Jurassic time scale of Gradstein et al. (2012). The 2σ full external uncertainty age obtained for the impact (206.91 ± 0.32 Ma) overlaps with a period of reverse magnetic polarity (white bars), and is thus consistent with the reversed polarity of melt-bearing rocks from the structure (Eitel et al. 2014). This figure also demonstrates that the Rochechouart impact is considerably older (5.6 ± 0.4 Ma) than the Triassic–Jurassic boundary.

known impact event coincident with the Triassic–Jurassic boundary. Flood basalt volcanism in the Central Atlantic Magmatic Province, which has been dated by both zircon U-Pb and basalt $^{40}Ar/^{39}Ar$ as coincident with the extinction (Marzoli et al. 1999; Jourdan et al. 2009b; Blackburn et al. 2013; Guex et al. 2016), thus remains the leading explanation for the Triassic–Jurassic mass extinction.

One of the reasons why the Rochechouart impact was formerly considered as a potential cause for the Triassic–Jurassic extinction was the hypothesis that it was concordant with the following impact structures, from largest to smallest: Manicouagan (100 km diameter, Canada), Lake Saint Martin (40 km, Canada), Obolon (20 km, Ukraine), and Red Wing (9 km, USA) (Spray et al. 1998). Rochechouart has also been suggested to be potentially coeval with the 40–80 km diameter Puchezh-Katunki structure in Russia (Schmieder et al. 2010). Subsequently, the ages for many of these structures have been redetermined, allowing for re-evaluation of this multiple impact hypotheses (e.g., Jourdan et al. 2012; Schmieder et al. 2014). The most accurate ages presently available for these impacts are, from oldest to youngest: Lake Saint Martin, 227.8 ± 0.9 Ma ($^{40}Ar/^{39}Ar$; Schmieder et al. 2014); Manicouagan, 215.56 ± 0.05 Ma (U-Pb ID-TIMS, Ramezani et al. 2006); Red Wing, 220–200 Ma (stratigraphy; Koeberl et al. 1996); Puchezh-Katunki, 192.0 ± 0.8 Ma ($^{40}Ar/^{39}Ar$; Holm-Alwmark et al. 2016); and Obolon, <185 Ma (stratigraphy; Schmieder and Buchner 2008). In light of our new $^{40}Ar/^{39}Ar$ age, the only known impact that may be coeval with Rochechouart is Red Wing—but this structure is very small and its age is imprecise.

Our revised $^{40}Ar/^{39}Ar$ age can also be used to examine potential temporal links between the Rochechouart impact and regional geological events. In particular, the Rochechouart impact has been hypothesized as the cause of earthquake and tsunami deposits found across >250,000 km^2 of the United Kingdom (Simms 2002, 2007) and possible correlated units elsewhere in Europe (Schmieder et al. 2010). The seismite and tsunamite horizon in the United Kingdom occurs within the upper Rhaetian portion of the Lilstock Formation, within the Penarth Group (Simms 2002, 2007). The Rhaetian extends from 209.5 to 201.3 Ma (Gradstein et al. 2012) and therefore the tsunamite and seismite horizon could be coincident in age with the Rochechouart impact. However, the seismite and tsunamite horizon is not precisely dated; unfortunately, all currently mapped localities have an erosional hiatus in the stratigraphic sequence, representing an undetermined length of time between the seismite and tsunamite horizon and the Triassic–Jurassic boundary (Simms 2002, 2007). Nevertheless, the seismite and tsunamite horizon is demonstrably below the Triassic–Jurassic boundary, defined in the field by the first appearance of the ammonite *Psiloceras* (Gradstein et al. 2012). The stratigraphic distance between the Triassic/Jurassic boundary and the tsunamite and seismite horizon differs between sites, likely due to varying sedimentation rates and/or contrasting amounts of missing sedimentation during the erosional hiatus. The distance between the first appearance of *Psiloceras* and the seismite and tsunamite horizon is 12.6 m at Larne, 7.4 m at Lavernock, 8.8 m at St. Audrie's Bay, and ~1.5 m at Manor Farm (Simms 2002). In the Mochras borehole, northwest Wales, soft-sediment deformation occurs 18–20 m below the first appearance of *Psiloceras* (Simms 2007). We suggest that more precise control on the age of the seismite and tsunamite horizon will be invaluable to further evaluate whether this aerially widespread deposit was caused by the Rochechouart impact.

The increased precision now available from $^{40}Ar/^{39}Ar$ analysis of Rochechouart also allows testing of time scales pertaining to the impact itself—in particular the longevity of hydrothermal activity and cooling. This is possible because impact products deposited near the surface would have cooled rapidly

postimpact (with only brief or no hydrothermal activity), whereas shocked basement rocks deep beneath the crater will have remained at elevated temperatures well after the impact event, forming widespread hydrothermal systems at depth (Osinski et al. 2013). The longevity of hydrothermal systems associated with impact craters can therefore be examined by the comparison of shallow versus deep samples (e.g., Schmieder and Jourdan 2013). Such analyses are now available in the case of Rochechouart. Our $^{40}Ar/^{39}Ar$ age from the Babaudus impact melt rock provides a suitable near-surface sample. Meanwhile, the rock analyzed by Schmieder et al. (2010) was sourced from beneath the crater, and comprised two separates of K-feldspar precipitated by hydrothermal solutions within an impact-metamorphosed gneiss.

The other samples previously analyzed from Rochechouart (Table 1) are less useful for the purpose of determining the duration of hydrothermal activity. Specifically, the three K-Ar ages were likely to have been affected by considerable Ar loss and would therefore be too young—especially as all of $^{40}Ar/^{39}Ar$ step-heating analyses indicate considerable Ar loss in the low-temperature steps (this study; Schmieder et al. 2010). The $^{40}Ar/^{39}Ar$ spot fusion age from pseudotachylitic breccia veins (Kelley and Spray 1997) is likely to be too old due to the presence of extraneous argon trapped in partially undegassed basement clasts and mineral fragments contained in the samples analyzed (as discussed by Schmieder et al. 2010, 2014). Meanwhile, the Rb-Sr and fission track analyses are insufficiently precise (Table 1), and while the reversed polarity measurements of the impact melt-bearing breccias do provide a useful age constraint (Fig. 6) (Eitel et al. 2014), the paleomagnetic results do not provide a precise numerical age for the impact.

The $^{40}Ar/^{39}Ar$ ages for the "shallow" versus "deep" samples at Rochechouart (i.e., this study and Schmieder et al. 2014, respectively) differ by 4 ± 2 Ma, which at face value would indicate cooling beneath Rochechouart might have extended over at least 2 Ma. For comparison, at the ~23 km wide Lappäjrvi impact structure (Finland), $^{40}Ar/^{39}Ar$ cooling ages span over 1.1 ± 0.5 Ma, potentially indicating cooling and hydrothermal activity extended for 0.6 Ma up to a maximum of 1.6 Ma (Schmieder and Jourdan 2013). However, a > 2 Ma time span for hydrothermal activity and cooling beneath Rochechouart exceeds the duration predicted from thermal modeling of impact structures. For example, the longevity of hydrothermal activity associated with 180 km wide Chicxulub crater is modeled to have a duration of between 1.5 and 2.3 Ma (Abramov and Kring 2007). This modeled timeframe at Chicxulub is comparable to the age difference between shallow versus deep samples from Rochechouart, despite Chicxulub being a much larger impact event, with a correspondingly greater initial thermal perturbation due to the impact.

We emphasize that the shallow versus deep samples from Rochechouart were analyzed by different laboratories in different irradiations, so advise caution in using this age difference, and recommend further high-precision analyses from Rochechouart, preferably with all samples analyzed in the same laboratory, and from the same irradiation. Fortunately, an upcoming drilling campaign at Rochechouart (Lambert et al. 2016) is set to provide an excellent opportunity to obtain further samples to determine the longevity of the hydrothermal system. This goal is especially timely because the Rochechouart hydrothermal system has recently been demonstrated to have supported sulfur-reducing bacteria, presumably as part of a much larger impact-generated biosphere (Simpson et al. 2017). Further investigations of terrestrial impact hydrothermal systems will also provide valuable analogs for similar systems on Mars, which have been proposed as sites that could have hosted extraterrestrial life (Cockell 2006; Schwenzer and Kring 2009; Osinski et al. 2013; Schmieder and Jourdan 2013).

CONCLUSIONS

$^{40}Ar/^{39}Ar$ analysis of the Babaudus impact melt yields an age for the Rochechouart impact of $206.92 \pm 0.20/0.32$ Ma (2σ, full analytical/external uncertainties). This new age is consistent with the reversed magnetic polarity of the impactites, and is 5.6 ± 0.4 Ma older than the Triassic–Jurassic boundary. Thus, there are now no known large impact structures coincident with the Triassic–Jurassic boundary. The widespread Central Atlantic Magmatic Province flood basalts remain the most likely cause of the Triassic–Jurassic mass extinction. Nevertheless, the Late Triassic Rochechouart impact may still be genetically linked to the >250,000 km^2 seismite and tsunamite horizon found across the United Kingdom—although testing of this link requires better age control on these sedimentary rocks, which currently lack precise ages. The duration of the postimpact hydrothermal system at Rochechouart, which hosted sulfur-reducing bacteria, should be examined by coordinated redating of impactite and hydrothermal products from the structure.

Acknowledgments—The authors thank the Réserve Naturelle de l'Astroblème de Rochechouart–Chassenon for supplying the Babaudus sample, and allowing access for fieldwork, and to Philipe Lambert for field guidance

and advice. We are also grateful to the Barringer Crater Company for funds to support fieldwork by Sarah Simpson. We thank Ross Dymock and Peter Chung for $^{40}Ar/^{39}Ar$ and SEM assistance, respectively. We appreciate the detailed and constructive reviews by Jo-Anne Wartho and Fred Jourdan, and the editorial handling and comments by Gordon Osinski. B.E. Cohen was supported by STFC grant ST/N000846/1. The funds for $^{40}Ar/^{39}Ar$ dating were supplied by the SUERC Argon Isotope Facility. NERC are thanked for the continued funding of the Argon Isotope Facility.

Editorial Handling—Dr. Gordon Osinski

REFERENCES

Abramov O. and Kring D. A. 2007. Numerical modeling of impact-induced hydrothermal activity at the Chicxulub crater. *Meteoritics & Planetary Science* 42:93–112.

Barfod D. N., Mark D. F., Tait A., Dymock R. C., and Imlach J. 2014. Argon extraction from geological samples by CO2 scanning laser step-heating. *Geological Society, London, Special Publication* 378:79–90.

Blackburn T. J., Olsen P. E., Bowring S. A., McLean N. M., Kent D. V., Puffer J., McHone G., Rasbury E. T., and Et-Touhami M. 2013. Zircon U-Pb geochronology links the end-triassic extinction with the central atlantic magmatic province. *Science* 340:941–945.

Carporzen L. and Gilder S. A. 2006. Evidence for coeval Late Triassic terrestrial impacts from the Rochechouart (France) meteorite crater. *Geophysical Research Letters* 33: L19308.

Cockell C. S. 2006. The origin and emergence of life under impact bombardment. *Philosophical Transactions of the Royal Society B* 361:1845–1856.

Collins G. S., Kenkmann T., Osinski G. R., and Wünnemann K. 2008. Mid-sized complex crater formation in mixed crystalline-sedimentary targets: Insight from modeling and observation. *Meteoritics & Planetary Science* 43:1955–1977.

Eitel M., Gilder S. A., Kunzmann T., and Pohl J. 2014. Rochechouart impact crater melt breccias record no geomagnetic field reversal. *Earth and Planetary Science Letters* 387:97–106.

Giordano D., Romano C., Papale P., and Dingwell D. B. 2004. The viscosity of trachytes, and comparison with basalts, phonolites, and rhyolites. *Chemical Geology* 213:49–61.

Gradstein F. M., Ogg J. G., Schmitz M. D., and Ogg G. M. 2012. *The geologic time scale*. Amsterdam: Elsevier. 1144 p.

Guex J., Pilet S., Muntener O., Bartolini A., Spangenberg J., Schoene B., Sell B., and Schaltegger U. 2016. Thermal erosion of cratonic lithosphere as a potential trigger for mass-extinction. *Scientific Reports* 6:23168.

Holm-Alwmark S., Alwmark C., Lindström S., Ferrière L., Schersten A., Masaitis V. L., Mashchak M. S., and Naumov M. V. 2016. An Early Jurassic $^{40}Ar/^{39}Ar$ age for the Puchexh-Katunki impact structure (Russia)–No causal link to an extinction event (abstract #6171). 79th Annual Meeting of the Meteoritical Society.

Jourdan F., Renne P. R., and Reimold W. U. 2007a. The problem of inherited $^{40}Ar^*$ in dating impact glass by the $^{40}Ar/^{39}Ar$ method: Evidence from the Tswaing impact crater (South Africa). *Geochimica et Cosmochimica Acta* 71:1214–1231.

Jourdan F., Matzel J. P., and Renne P. R. 2007b. ^{39}Ar and ^{37}Ar recoil loss during neutron irradiation of sanidine and plagioclase. *Geochimica et Cosmochimica Acta* 71:2791–2808.

Jourdan F., Renne P. R., and Reimold W. U. 2009a. An appraisal of the ages of terrestrial impact structures. *Earth and Planetary Science Letters* 286:1–13.

Jourdan F., Marzoli A., Bertrand H., Cirilli S., Tanner L. H., Kontak D. J., McHone G., Renne P. R., and Bellieni G. 2009b. $^{40}Ar/^{39}Ar$ ages of CAMP in North America: Implications for the Triassic-Jurassic boundary and the ^{40}K decay constant bias. *Lithos* 110:167–180.

Jourdan F., Moynier F., Koeberl C., and Eroglu S. 2011. $^{40}Ar/^{39}Ar$ age of the Lonar crater and consequence for the geochronology of planetary impacts. *Geology* 39:671–674.

Jourdan F., Reimold W. U., and Deutsch A. 2012. Dating terrestrial impact structures. *Elements* 8:49–53.

Kelley S. and Spray J. G. 1997. A Late Triassic age for the Rochechouart impact structure, France. *Meteoritics & Planetary Science* 32:629–636.

Koeberl C., Reimold W. U., and Brandt D. 1996. Red Wing Creek structure, North Dakota: Petrographical and geochemical studies, and confirmation of impact origin. *Meteoritics & Planetary Science* 31:335–342.

Koppers A. A. P., Staudigel H., and Wijbrans J. R. 2000. Dating crystalline groundmass separates of altered Cretaceous seamount basalts by the $^{40}Ar/^{39}Ar$ incremental heating technique. *Chemical Geology* 166:139–158.

Koppers A. A. P., Yamazaki T., Geldmacher J., Gee J. S., Pressling N., Hoshi H., Anderson L., Beier C., Buchs D. M., Chen L. H., Cohen B. E., Deschamps F., Dorais M. J., Ebuna D., Ehmann S., Fitton J. G., Fulton P. M., Ganbat E., Hamelin C., Hanyu T., Kalnins L., Kell J., Machida S., Mahoney J. J., Moriya K., Nichols A. R. L., Rausch S., Sano S.-I., Sylvan J. B., and Williams R. 2012. Limited latitudinal mantle plume motion for the Louisville hotspot. *Nature Geoscience* 5:911–917.

Kraut F. and French B. M. 1971. The Rochechouart meteorite impact structure, France: Preliminary geological results. *Journal of Geophysical Research* 76:5407–5413.

Lambert P. 1974. La structure d'impact de météorite géante de Rochechouart. Ph.D thesis. Université de Paris-Sud, Paris, France.

Lambert P. 2010. Target and impact deposits at Rochechouart impact structure, France. *Geological Society of America, Special Paper* 465:509–541.

Lambert P., Goderis S., Hodges K. V., Kelley S., Lee M. R., Jourdan F., Osinski G. R., Sapers H. M., Schmieder M., Schwenzer S., Trumel H., and Wittmann A. 2016. Preparing the 2017 drilling campaign at Rochechouart impact structure (abstract). *Meteoritics & Planetary Science* 51 (Suppl.):A6471.

Lee J.-Y., Marti K., Severinghaus J. P., Kawamura K., Yoo H.-S., Lee J. B., and Kim J. S. 2006. A redetermination of the isotopic abundances of atmospheric Ar. *Geochimica et Cosmochimica Acta* 70:4507–4512.

Mark D. F., Barfod D., Stuart F. M., and Imlach J. 2009. The ARGUS multicollector noble gas mass spectrometer: Performance for $^{40}Ar/^{39}Ar$ geochronology. *Geochemistry, Geophysics, Geosystems* 10:Q0AA02.

Mark D. F., Stuart F. M., and de Podesta M. 2011. New high-precision measurements of the isotopic composition of atmospheric argon. *Geochimica et Cosmochimica Acta* 75:7494–7501.

Mark D. F., Lindgren P., and Fallick A. E. 2014. A high-precision $^{40}Ar/^{39}Ar$ age for hydrated impact glass from the Dellen impact, Sweden. *Geological Society, London, Special Publications* 378:349–366.

Marzoli A., Renne P. R., Piccirillo E. M., Ernesto M., Bellieni G., and De Min A. 1999. Extensive 200-million-year-old continental flood basalts of the Central Atlantic Magmatic Province. *Science* 284:616–618.

McDougall I. and Harrison T. M. 1999. *Geochronology and thermochronology by the $^{40}Ar/^{39}Ar$ method*. New York: Oxford University Press. 261 p.

McDougall I. and Wellman P. 2011. Calibration of GA1550 biotite standard for K/Ar and $^{40}Ar/^{39}Ar$ dating. *Chemical Geology* 280:19–25.

Morgan L. E., Mark D. F., Imlach J., Barfod D., and Dymock R. 2014. FCs-EK: A new sampling of the Fish Canyon Tuff $^{40}Ar/^{39}Ar$ neutron flux monitor. *Geological Society, London, Special Publications* 378:63–67.

Osinski G. R. and Pierazzo E. 2012. *Impact cratering: Processes and products*. Chichester, UK: Wiley-Blackwell.

Osinski G. R., Tornabene L. L., Banerjee N. R., Cockell C. S., Flemming R., Izawa M. R. M., McCutcheon J., Parnell J., Preston L. J., Pickersgill A. E., Pontefract A., Sapers H. M., and Southam G. 2013. Impact-generated hydrothermal systems on Earth and Mars. *Icarus* 224:347–363.

Pohl J. and Soffel H. 1971. Paleomagnetic age determination of the Rochechouart impact structure (France). *Zeitschrift fur Geophysik* 37:857–866.

Ramezani J., Bowring S. A., Pringle M. S., Winslow F. D. I., and Rasbury E. T. 2006. The Manicouagan impact melt rock: A proposed standard for the intercalibration of U-Pb and $^{40}Ar/^{39}Ar$ isotopic systems. *Geochimica et Cosmochimica Acta* 69:A301.

Reimold W. U. and Oskierski W. 1987. The Rb-Sr-age of the Rochechouart impact structure, France, and geochemical constraints on impact melt-target rock-meteorite compositions. In *Research in terrestrial impact structures*, edited by Pohl J. Braunschweig, Germany: Friedr. Vieweg & Sohn. pp. 94–114.

Renne P. R., Balco G., Ludwig K. R., Mundil R., Min K. 2011. Response to the comment by W.H. Schwarz et al. on "Joint determination of ^{40}K decay constants and $^{40}Ar^*/^{40}K$ for the Fish Canyon sanidine standard, and improved accuracy for $^{40}Ar/^{39}Ar$ geochronology" by Paul R. Renne et al. (2010). *Geochimica et Cosmochimica Acta* 75:5097–5100.

Rohde R. A. and Muller R. A. 2005. Cycles in fossil diversity. *Nature* 434:208–201.

Rotenberg E., Davis D. W., Amelin Y., Ghosh S., and Bergquist B. A. 2012. Determination of the decay-constant of ^{87}Rb by laboratory accumulation of ^{87}Sr. *Geochimica et Cosmochimica Acta* 85:41–57.

Sapers H. M., Osinski G. R., Banerjee N. R., Ferrière L., Lambert P., and Izawa M. R. M. 2014. Revisiting the Rochechouart impact structure, France. *Meteoritics & Planetary Science* 49:2152–2168.

Schmieder M. and Buchner E. 2008. Dating impact craters: Palaeogeographic versus isotopic and stratigraphic methods—A brief case study. *Geological Magazine* 145:586–590.

Schmieder M. and Jourdan F. 2013. The Lappajärvi impact structure (Finland): Age, duration of crater cooling, and implications for early life. *Geochimica et Cosmochimica Acta* 112:321–339.

Schmieder M., Buchner E., Schwarz W. H., Trieloff M., and Lambert P. 2010. A Rhaetian $^{40}Ar/^{39}Ar$ age for the Rochechouart impact structure (France) and implications for the latest Triassic sedimentary record. *Meteoritics & Planetary Science* 45:1225–1242.

Schmieder M., Jourdan F., Tohver E., and Cloutis E. A. 2014. $^{40}Ar/^{39}Ar$ age of the Lake Saint Martin impact structure (Canada)—Unchaining the Late Triassic terrestrial impact craters. *Earth and Planetary Science Letters* 406:37–48.

Schoene B., Guex J., Bartolini A., Schaltegger U., and Blackburn T. J. 2010. Correlating the end-Triassic mass extinction and flood basalt volcanism at the 100 ka level. *Geology* 38:387–390.

Schwenzer S. P. and Kring D. A. 2009. Impact-generated hydrothermal systems capable of forming phyllosilicates on Noachian Mars. *Geology* 37:1091–1094.

Simms M. J. 2002. Uniquely extensive seismite from the latest Triassic of the United Kingdom: Evidence for bolide impact? *Geology* 31:557–560.

Simms M. J. 2007. Uniquely extensive soft-sediment deformation in the Rhaetian of the UK: Evidence for earthquake or impact? *Palaeogeography, Palaeoclimatology, Palaeoecology* 244:407–423.

Simpson S. L., Boyce A. J., Lambert P., Lindgren P., and Lee M. R. 2017. Evidence for an impact-induced biosphere from the $\delta^{34}S$ signature of sulphides in the Rochechouart impact structure, France. *Earth and Planetary Science Letters* 460:192–200.

Smith R. 2011. Lost world: Did a giant impact 200 million years ago trigger a mass extinction and pave the way for the dinosaurs? *Nature* 479:287–289.

Spray J. G., Kelley S. P., and Rowley D. B. 1998. Evidence for a Late Triassic multiple impact event on Earth. *Nature* 392:171–173.

Stöffler D. and Grieve R. A. F. 2011. Impactites. In *Metamorphic rocks: A classification and glossary of terms*, edited by Fettes D. and Desmons J. Cambridge, UK: Cambridge University Press. pp. 82–92.

Wagner G. A. and Storzer D. 1975. The age of the Rochechouart structure. *Meteoritics* 10:503–504.

Webb A. W. and McDougall I. 1967. A comparison of mineral and whole rock potassium-argon ages of Tertiary volcanics from central Queensland, Australia. *Earth and Planetary Science Letters* 3:41–47.

SUPPORTING INFORMATION

Additional supporting information may be found in the online version of this article:

Table S1: Microsoft Excel file containing $^{40}Ar/^{39}Ar$ analytical data.